ICAS 2016
30th Congress of the International Council of the Aeronautical Sciences
DCC, Daejeon, Korea ; September 25-30, 2016

EULERIAN METHOD FOR IN-ENGINE ICING: WITH APPLICATION TO ICE CRYSTAL TRAJECTORIES AND IMPACT IN A GENERIC TURBOFAN COMPRESSOR

E. Norde*, E.T.A. van der Weide*, H.W.M. Hoeijmakers*
***University of Twente, Enschede, The Netherlands**

Keywords: *Ice crystals, Eulerian, Multiphase, Impingement, In-engine icing*

Abstract

In this study an Eulerian method is utilized to compute trajectories of ice crystals and their impact in a stator-rotor-stator cascade. On their trajectories the (non-spherical) ice particles are subject to evaporation/sublimation and melting and they will deposit either fully or partially on the blade surface. Results of the total water content, melting ratio and impinging mass flux will be compared for particles of different size.

1 Introduction

This research is carried out in the framework of project High Altitude Ice Crystals (HAIC) [1] funded by the European Union. HAIC started in 2012 and brings together more than 30 European and 5 International partners. The project aims at improving the understanding power loss and damage of jet engines caused by ice crystals. To that aim the project develops ice crystal detection and awareness technologies, test facilities and numerical capabilities. Ice crystal icing is a major concern regarding aviation safety as is clear from the recently updated database of events caused by in-engine ice crystal icing: 162 events occurred in the period 1990-2014 [2].
To understand the process of ice crystal icing a numerical method for ice crystal trajectories and impact has been developed at the University of Twente. In the first part of this paper the numerical method and the theory behind the particle motion and wall interactions is introduced. In the second part the method is applied to a cascade, representing a generic turbofan compressor. Results will be shown for ice particles of different size travelling through this cascade while being subject to phase change and wall impact.

2 Numerical method

The numerical method is a further development of two computational methods: (1) Droplerian [3], an in-house Eulerian method for ice accretion due to super-cooled large droplets (SLD), and (2) an in-house multi-block flow solver. The resulting method is referred to as MooseMBIce: Multi-disciplinary Object oriented Optimization and Simulation Environment for Multi-Block structured Ice accretion. MooseMBIce employs a cell-centered finite-volume discretization with second-order spatial accuracy. An upwind method using an approximate Riemann solver with a van Leer limiter is applied. Time integration is performed by a standard low-storage four-stage Runge-Kutta scheme using local time stepping in steady flow solutions.

3 Eulerian trajectory method

In ice crystal icing there is emphasis on the shape of the ice crystal and its ability to evaporate or melt when travelling through a warm environment. Furthermore, the co-existence of ice and water results in complex physics governing the bouncing, sticking or splashing processes of the ice crystals at the surface of impact. A detailed analysis of the theoretical models applied to the particle trajectories and impact has already been provided by the authors in a previous paper

(Norde, Van der Weide and Hoeijmakers, 2016) [4]. The models and main assumptions will be repeated briefly.

3.1 Trajectories melting ice crystals

The governing equations for mass, momentum and energy are given in Eq. (1)-(4). If the ice crystal has partially melted and the particle consists of both ice and water, a continuity equation has to be solved for each of these two phases. This formulation is based on the assumptions that the particle flow can be treated as a dilute continuum phase and that one-way coupling exists between the dispersed phase and the air flow.

$$\frac{\partial \alpha_i}{\partial t} + \nabla \cdot (\alpha_i \mathbf{v}) = -S_S - S_{M|I} \tag{1}$$

$$\frac{\partial \alpha_w}{\partial t} + \nabla \cdot (\alpha_w \mathbf{v}) = -S_E + S_{M|W} \tag{2}$$

$$\frac{\partial \alpha \mathbf{v}}{\partial t} + \nabla \cdot (\alpha \mathbf{v}\mathbf{v}) = S_D + S_G \tag{3}$$

$$\frac{\partial \alpha T}{\partial t} + \nabla \cdot (\alpha T \mathbf{v}) = S_C + S_E S_{L|E} + S_S S_{L|S} + S_A \tag{4}$$

where α_i is the ice volume fraction, α_w is the water volume fraction, α (= α_i+α_w) is the total particle volume fraction, $\mathbf{v}$ is the particle velocity and T is the particle temperature.

The quantities denoted by S are the source terms related to sublimation S_S, evaporation S_E, melting S_M, drag S_D, gravity S_G, convection heat transfer S_C and latent heat S_L. S_A is an additional term that assures that the energy is conserved during melting and that the particle temperature is kept at the melting temperature by correcting for the small fraction of water that evaporates. The drag and gravity source term hold for all particle temperatures and are given by:

$$S_D = \frac{3\mu_a C_d(\mathrm{Re},\Phi)\mathrm{Re}}{4\Phi\rho_p d_p^2}\alpha(\mathbf{v}_a - \mathbf{v}) \tag{5}$$

$$S_G = \left(1 - \frac{\rho_a}{\rho_p}\right)\alpha\mathbf{g} \tag{6}$$

The drag coefficient C_d, given in Eq. (7), is obtained by a correlation proposed by Ganser [5]. This correlation depends on the particle sphericity Φ and the crosswise sphericity $\Phi_\perp$, in the form of a Stokes shape factor K_1 and a Newton shape factor K_2.

$$C_D = \frac{24}{\mathrm{Re}K_1}\left(1 + 0.1118(\mathrm{Re}K_1K_2)^{0.6567}\right) + \frac{0.4305K_2}{1 + \frac{3305}{\mathrm{Re}K_1K_2}}, \quad \text{for} \quad \mathrm{Re}K_1K_2 \le 10^5 \tag{7}$$

where

$$K_1 = \left(\frac{1}{3}\Phi_\perp^{-1/2} + \frac{2}{3}\Phi^{-1/2}\right)^{-1}$$

$$K_2 = 10^{1.8148(-\log\Phi)^{0.5743}}$$

The particle sphericity and crosswise sphericity are defined as:

$$\Phi = \frac{\pi d_p^2}{A_p}, \quad \Phi_\perp = \frac{(1/4)\pi d_p^2}{A_{proj}} \tag{8}$$

where A_p is the surface area of the particle and A_{proj} is the area of the projected surface of the particle perpendicular to the flow. The particle Reynolds number is given by:

$$\mathrm{Re} = \frac{\rho_a d_p |\mathbf{v}_a - \mathbf{v}|}{\mu_a} \tag{9}$$

The other symbols in Eq. (5)-(9) represent the dynamic viscosity of air μ_a, the particle density ρ_p, the particle equivalent diameter d_p, the air density ρ_a, the air velocity $\mathbf{v}_a$ and the gravitational acceleration $\mathbf{g}$.

The remaining source terms in Eq. (1)-(4) depend on the particle temperature.

(i) If the particle temperature is below the melting temperature T_m, only ice is present and the particle can either increase in temperature and/or sublimate.

$$S_S = \frac{6\rho_a D_v \mathrm{Sh}(\mathrm{Re},\Phi)}{\Phi\rho_i d_p^2}\alpha_i(y_{vp} - y_{vg}) \tag{10}$$

$$S_C = \frac{6k_a \mathrm{Nu}(\mathrm{Re},\Phi)}{\Phi\rho_i c_{p,i} d_p^2}\alpha_i(T_a - T) \tag{11}$$

$$S_{L|S} = \frac{L_s}{c_{p,i}}\alpha_i \tag{12}$$

(ii) If the particle temperature is above the melting temperature, only water is present and the particle can either continue to increase in temperature and/or evaporate. The particle sphericity is assumed to be equal to one in this case.

$$S_E = \frac{6\rho_a D_v \mathrm{Sh}(\mathrm{Re},\Phi)}{\rho_w d_p^2}\alpha_w(y_{vp} - y_{vg}) \tag{13}$$

$$S_C = \frac{6k_a \mathrm{Nu}(\mathrm{Re},\Phi)}{\rho_w c_{p,w} d_p^2}\alpha_w (T_a - T) \quad (14)$$

$$S_{L|E} = \frac{L_v}{c_{p,w}}\alpha_w \quad (15)$$

(iii) The melting phase, in which the particle temperature equals the melting temperature, is described by the model introduced by Mason [6]. Mason assumes that the latent heat of melting equals the sum of the conduction through the air and the condensation of vapor on the surface. The particle will retain the melting temperature uniformly through the ice core and the water layer and the water layer is non-shedding and uniformly distributed around the ice core. This results in the additional source terms governing the melting process.

$$S_{M|I} = \frac{6k_a \mathrm{Nu}(\mathrm{Re},\Phi)}{\Phi\rho_i d_p^2 L_m}\alpha_i (T_a - T_m) + \frac{6\rho_a D_v \mathrm{Sh}(\mathrm{Re},\Phi)}{\Phi\rho_i d_p^2}\frac{L_v}{L_m}\alpha_i (y_{vp} - y_{vg}) \quad (16)$$

$$S_{M|W} = S_{M|I} - \frac{6\rho_a D_v \mathrm{Sh}(\mathrm{Re},\Phi)}{\Phi\rho_w d_p^2}\alpha_w (y_{vp} - y_{vg}) \quad (17)$$

$$S_A = \frac{6\rho_a D_v \mathrm{Sh}(\mathrm{Re},\Phi)}{\Phi\rho_w d_p^2}\alpha_w (y_{vp} - y_{vg}) T_m \quad (18)$$

The new symbols introduced in Eq. (10)-(18) are the water vapor diffusivity in air D_v, the vapor mass fraction at the particle surface y_{vp}, the free-stream vapor mass fraction y_{vg}, the density of ice and water, ρ_i and ρ_w, respectively, the thermal conductivity of air k_a, the specific heat of ice and water, $c_{p,i}$ and $c_{p,w}$, respectively, the latent heat of sublimation, evaporation and melting, L_s, L_v, and L_m, respectively, and the melting temperature T_m. For the Nusselt number Nu(Re,Φ), given in Eq. (19), a correlation derived by Trontin et al. [7] has been used which depends on the particle Reynolds number and the particle sphericity Φ. The Sherwood number Sh(Re,Φ), Eq. (20), is linked to the Nusselt number by the Chilton-Colburn analogy.

$$\mathrm{Nu} = 2\sqrt{\Phi} + 0.55\,\mathrm{Pr}^{1/3}\Phi^{1/4}\sqrt{\mathrm{Re}} \quad (19)$$

$$\mathrm{Sh} = 2\sqrt{\Phi} + 0.55\mathrm{Sc}^{1/3}\Phi^{1/4}\sqrt{\mathrm{Re}} \quad (20)$$

The Prandtl number Pr is set to the typical value for air (Pr = 0.71) and the vapor Schmidt number Sc is defined as the ratio of diffusion of momentum to diffusion of mass:

$$Sc = \frac{\mu_a}{\rho_a D_v} \quad (21)$$

During a phase change the ice crystal will undergo a change in size and sphericity. The particle sphericity Φ is assumed constant during the sublimation and evaporation process. During melting Φ will be non-linearly interpolated between the initial value Φ_0 for the ice particle and 1 for the melted particle:

$$\Phi = \left(\frac{\alpha_i}{\alpha_i + \alpha_w}\right)\Phi_0 + \left[1 - \left(\frac{\alpha_i}{\alpha_i + \alpha_w}\right)\right] \quad (22)$$

The particle size d_p is obtained by an additional equation for the particle number density n:

$$\frac{\partial n}{\partial t} + \nabla\cdot(n\mathbf{v}) = 0, \quad \text{where } n = \frac{\alpha_i + \alpha_w}{(\pi/6)d_p^3} \quad (23)$$

3.2 Ice crystal impingement

3.2.1 Impact model

In MooseMBIce an impact model described by Trontin et al. [7] is applied. On impact with a surface ice crystals are allowed to bounce, stick or fragment into smaller particles depending on a dimensionless number L.

$$L = \frac{\rho_p d_p v_n^2}{e_\sigma} \quad (24)$$

Here v_n is the normal component of the particle velocity and e_σ is the surface energy, given by:

$$e_\sigma = e_{\sigma 0}\exp\left[\frac{Q_s}{R}\left(\frac{1}{T} - \frac{1}{T_0}\right)\right] \quad (25)$$

In this equation the initial surface energy $e_{\sigma 0}$ is assumed to be 0.12 J/m^2 at T_0 of 253 K, the activation energy Q_s is assumed to be 48.2 kJ/mol and R is the gas constant.

L can be seen as the ratio of the impact kinetic energy and the surface energy. The threshold values restricting the impact regimes have been validated by, amongst others, recent experiments by Hauk [8] and are set to be:

$$L_{c1} = 0.5, \qquad L_{c2} = 90 \quad (26)$$

This results in the impact model having three possible regimes:

$L \le L_{c1}$	elastic bouncing
$L_{c1} < L < L_{c2}$	inelastic bouncing, crack formation within the particle
$L \ge L_{c2}$	fragmentation

The probability that a particle will stick to the wall depends on the amount of liquid that is present. This can be liquid in the form of a thin layer already present on the wall or liquid present as melted water surrounding the particle's ice core. Trontin et al. [7] have defined the deposition probability P_D to be:

$$P_D = 1 - \min\left[1, K_B \xi_{nn}^2 \left(\delta_p + \delta_w\right)^{-1/3}\right] \quad (27)$$

In this equation δ_p and δ_w are the dimensionless particle film thickness and wall film thickness, respectively, and ξ_{nn}, which is a function of parameter L, is the normal restitution coefficient which is defined in Eq. (31). Parameter K_B has been fitted to experimental data and has a value of 40.

In case of a bouncing or shattering event the number of particles that stick to the wall equals P_D times the mass flux: $P_D(\rho_p \alpha) v_n$. The rebounded part equals:

$$\alpha_s v_{ns} = \left(1 - P_D\right) \alpha v_n \quad (28)$$

where the subscript s stands for the properties of the secondary particles. Furthermore, Trontin et al. [7] have also defined the remaining characteristics of the secondary particles including the secondary particle diameter $d_{p,s}$, secondary particle sphericity Φ_s and the secondary particle velocity $\mathbf{v}_s$. In case of a rebound event the secondary diameter and sphericity equal the diameter and sphericity of the particles in the parent cloud. In case of a fragmentation event the diameter and sphericity of the secondary particles depend on a random number R. R_d has a value between 0 and 1 and R_Φ has a value between 0.7 and 0.9. The characteristics of the secondary particles are summarized in Table 1.

Table 1a. Characteristics bounced particle.

Bounced particle	
Diameter, $d_{p,s}$	d_p
Sphericity, Φ_s	Φ
Velocity, $\mathbf{v}_s$	$\xi_t\left(\mathbf{v} - \left(\mathbf{v}\cdot\mathbf{n}\right)\mathbf{n}\right) - \xi_{nn}\left(\mathbf{v}\cdot\mathbf{n}\right)\mathbf{n}$

Table 1b. Characteristics fragmented particle.

Fragmented particle	
Diameter, $d_{p,s}$	$R_d\left(\frac{L_{c2}}{L}\right)^{2/11} d_p$
Sphericity, Φ_s	R_Φ
Velocity, $\mathbf{v}_s$	$\xi_t\left(\mathbf{v} - \left(\mathbf{v}\cdot\mathbf{n}\right)\mathbf{n}\right) - \left(\mathbf{v}\cdot\mathbf{n}\right)\left(\xi_{nt}\mathbf{t} + \xi_{nn}\mathbf{n}\right)$

The tangential restitution coefficient ξ_t and the normal restitution coefficients ξ_{nt} and ξ_{nn} are given by:

$$\xi_t = 1 \quad (29)$$

$$\xi_{nt} = 0.4\left(1 - \sqrt{\frac{L_{c2}}{L}}\right) \quad (30)$$

$$\xi_{nn} = \begin{cases} 1 & \text{if } L \le L_{c1} \\ \left(\frac{L_{c1}}{L}\right)^{1/3} & \text{if } L > L_{c1} \end{cases} \quad (31)$$

Here ξ_{nt} is the fraction of the normal momentum that is transferred into tangential momentum and ξ_{nn} is the fraction of normal momentum that is transferred into normal momentum.

3.2.2 Poly-dispersion

Now that the impact model has been described, the secondary particle flow has to be treated in such a way that it does not influence the parent particle cloud. The co-existence of particles that differ in size and/or velocity will lead to convergence issues when applying an Eulerian approach. The resulting particle size or velocity will be an averaged value and this will lead to solutions that are physically incorrect. A way to solve this trajectory crossing is to inject the secondary particles into new particle classes or bins. The parent cloud calculation is carried out first and the catching efficiency of the impinging particles on the surface will be reduced by the fraction of particles that rebound or fragment. Subsequently, the secondary cloud is computed, starting from the bin containing the largest fragments. The secondary particle characteristics are set as inlet condition on the impact surface and the far-field values are set to zero. This computation will continue until particles from the smallest bin have been treated. In case of multiple re-impingements of particles further downstream another secondary

cloud computation has to be performed. The process of particle re-injection is shown schematically in Fig. 1. Here subscripts r and f refer to rebounded and fragmented fractions of the parent cloud, respectively.

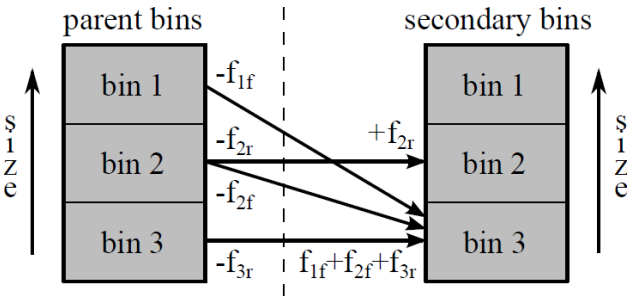

Fig. 1. Particle re-injection.

4 Compressor test case

A test case has been designed to analyze the flow of ice particles in an engine-like geometry. This test case has also been used to validate the achievement of Technology Readiness Level 4 (TRL4) of the numerical tools developed within HAIC.

4.1 Geometry

The test case consists of a 1.5-stage stator-rotor-stator linear cascade originally designed at Duke University [9]. A similar configuration has been used in research of, amongst others, Gopinath et al. [10] and Giangaspero [11]. The blade ratios equal 16:20:25 and the chord of the rotor blade is set to 4 cm. The annular radius of the cascade is set very large ($r/c_{rotor} \approx 254$) such that the configuration can be seen as two-dimensional. This accommodates flow solvers that cannot handle periodic boundary conditions in the circumferential direction. At the inlet the stagnation pressure, stagnation temperature and the velocity are prescribed and at the outlet the static pressure is prescribed. The grid is linearly cascaded using periodic boundary conditions and the hub and casing in z-direction are modeled as solid walls. The sliding interfaces are modeled as mixing planes which allows a steady state analysis, see Fig. 2. The grid consists of 9964, 6592 and 12160 cells for stator 1, rotor and stator 2, respectively.

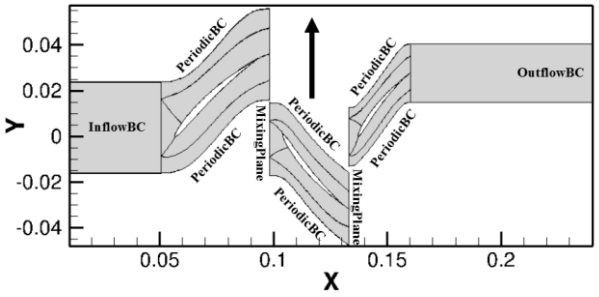

Fig. 2. Schematic stator-rotor-stator configuration with boundary conditions.

4.2 Aerodynamic flow field

The air flow field has been obtained employing the Euler equations for steady flow. The aerodynamic inlet conditions and exhaust static pressure are listed in Table 2. The inlet velocity has been set at an incidence angle of 53°, which can be caused by, for instance, a fan upstream of the first stator. The Mach and temperature contour fields are shown in Fig. 3 and Fig. 4, respectively. The aerodynamic conditions are set such that some ice particle melting is to be expected.

Table 2. Aerodynamic conditions cascade.

Mach M_∞	0.25
p_{total}	38750 Pa
T_{total}	296 K
v_{rotor}	140 m/s
Relative humidity	25 %
$p_{static,exhaust}$	40472 Pa

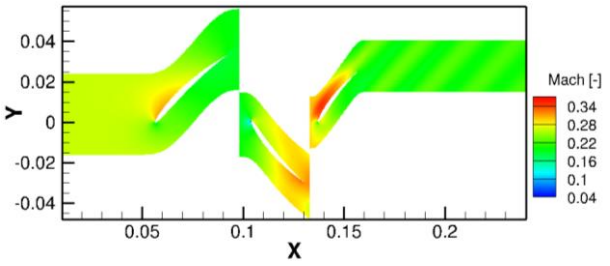

Fig. 3. Mach number field.

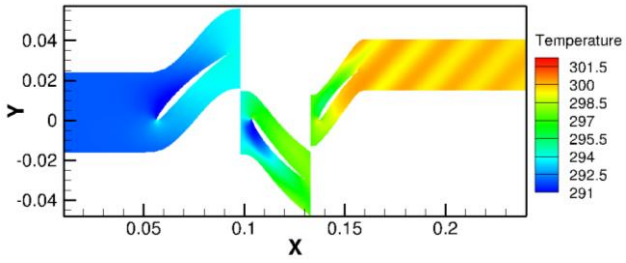

Fig. 4. Temperature field.

5 Results

Computations have been performed for two particles of spheroidal shape:

- run a, d_p = 50 µm, $\Phi,\Phi_\perp$ = 0.7
- run b, d_p = 20 µm, $\Phi,\Phi_\perp$ = 0.7.

Other physical properties have been kept the same and their values are listed in Table 3.
One set of computations is performed with the impact model de-activated (full deposition mode) and the computations for run b have been repeated with the impact model active (partial deposition mode).

Table 3. Particle properties.

Total Water Content (TWC)	2 g/m^3
T	268 K
ρ_i	917 kg/m^3
ρ_w	999.8 kg/m^3

5.1 Impact model de-activated

The results for runs a and b in full deposition mode are shown in Fig. 5-12. Fig. 5-8 show the 2D fields in the central plane of the Total Water Content (TWC) and the particle melting ratio. Fig. 9-12 contain the values of the particle's impinging mass flux and melting ratio along each blade's normalized curvilinear abscissa.
The TWC contour field for the large particles, Fig. 5, is very similar to that for the small particles, Fig. 6. From the inlet to the outlet of the cascade the TWC decreases from 2 g/m^3 to approximately 1 g/m^3, primarily because of particles remaining on the blade surface. In the shadow areas (dark blue) no or only a few particles reside and these regions of low concentration are subject to dissipation in the outlet part of the cascade resulting in the interface to become less sharp. The shadow areas around the blades are slightly smaller for the smaller particles. Smaller particles will follow the air streamlines more closely than larger particles and smaller particles are better able to follow the curvature of the blade. From the surface contours of the impinging mass flux, Fig. 9-11, it can be seen that the particles impact:

- on the pressure side of the first stator
- on the pressure side of the rotor
- on the suction side of the second stator.

A portion of the small particles, however, is able to follow the curvature of the pressure side of the second stator almost up to the trailing edge of the pressure side of this stator. The majority of the large particles impacts on the first stator and only a small portion impacts on the second stator or leaves the cascade without impacting at all. Compared to the large particles, the smaller particles impinge on blades further downstream in the cascade as a smaller fraction impacts the first stator and a larger fraction impacts the rotor.
The (dark blue) shadow zones in Fig. 5 and 6 are absent in the field of the particle melting ratio, Fig. 7 and 8. This is because the Eulerian computation is solved for conservative variables and the primitive variables still have a (sometimes inaccurate) value because of the threshold value of 1e-9*TWC that is set in the shadow zones to prevent the local density from becoming zero. The melting ratio for run a reaches 0.08 at the outlet and for run b it reaches a maximum value of 0.45. As would be expected, the smaller particles are more prone to melting and from Fig. 12 it can be seen that the melting ratio along the blades differs almost a factor 8 comparing the results for the large and those for the small particles.

5.2 Impact model activated

In this section the results for run b, the small particles, obtained for the partial deposition mode will be discussed. The bin distribution for the secondary particles consists of four different sizes: 20 µm, 15 µm, 10 µm and 5 µm. This implies that the fragmented particles will be injected in the secondary bin with the diameter closest to that of the secondary particle diameter obtained from the impact model. In the next section some issues within the Eulerian approach will be addressed.

5.2.1 Difficulties with Eulerian method

The Eulerian method can only handle one particle size and velocity per grid cell, as was already mentioned in Section 3.2.2. The periodic boundaries in the linear cascade introduce the possibility of crossing trajectories which causes the computation to diverge.

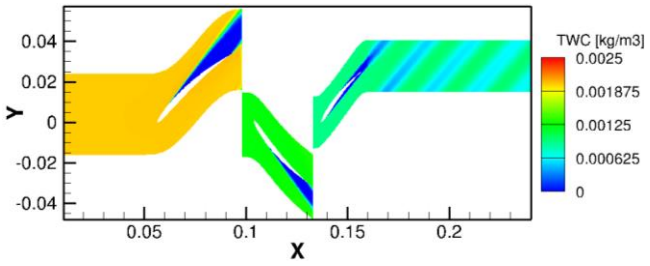

Fig. 5. TWC field run 1a, d_p = 50 µm.

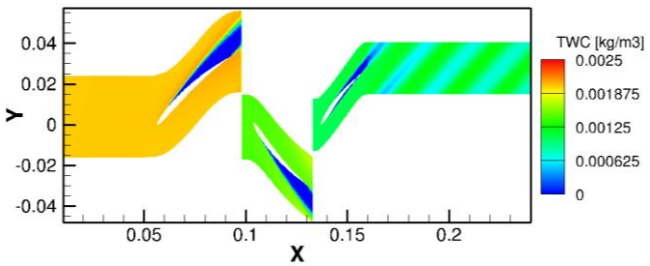

Fig. 6. TWC field run 1b, d_p = 20 µm.

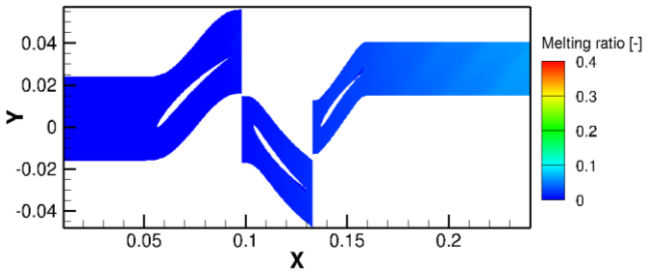

Fig. 7. Melting ratio field run 1a, d_p = 50 µm.

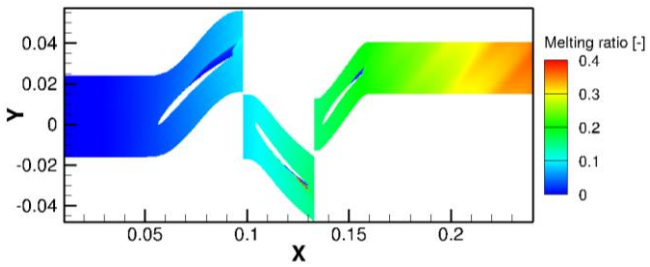

Fig. 8. Melting ratio field run 1b, d_p = 20 µm.

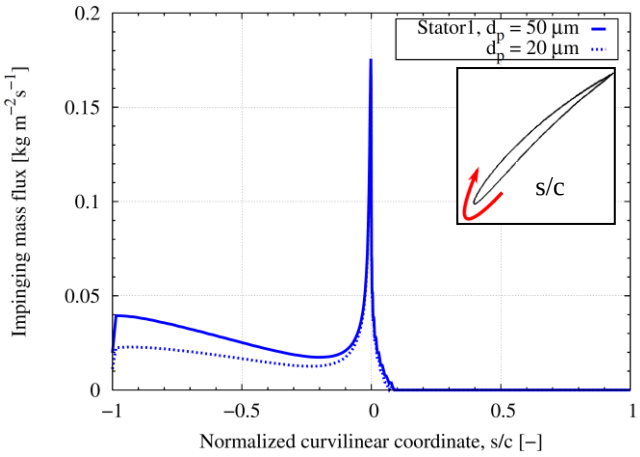

Fig. 9. Mass flux along stator 1.

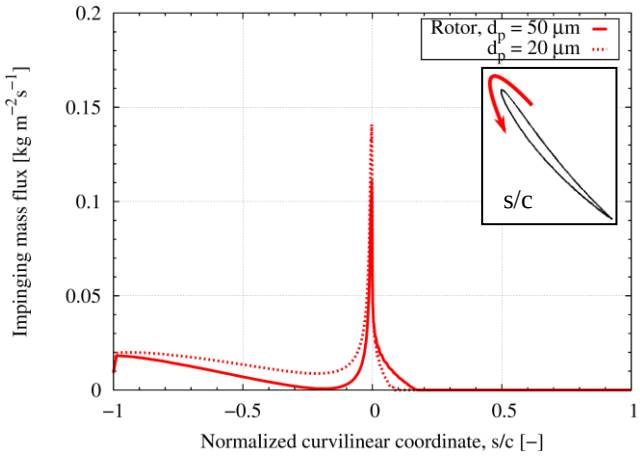

Fig. 10. Mass flux along rotor.

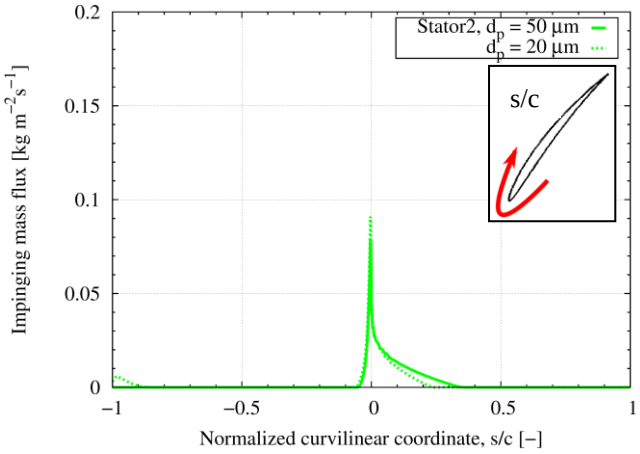

Fig. 11. Mass flux along stator 2.

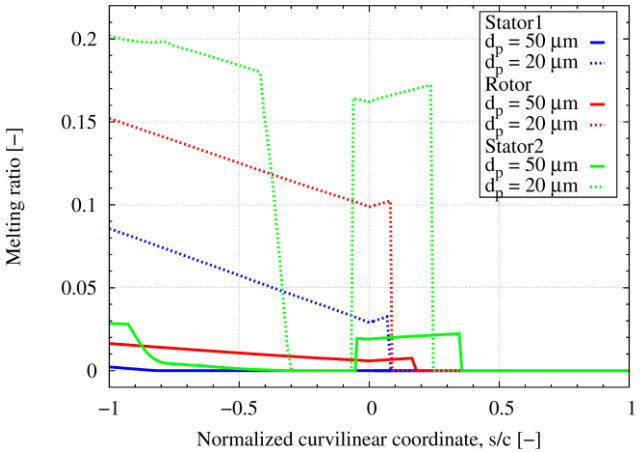

Fig. 12. Melting ratio along blades.

Crossing of particle trajectories is omitted by introducing additional bins that handle the pressure and suction surface of each blade separately. So, instead of *n* secondary bins, now 6*n* secondary bins are solved for either surface of the three rows of blades. Re-impingement of rebounding or particles from shattering in an upstream blade row is taken into account in a new iteration of the secondary cloud.
Another problem arises by the impact model itself. At the leading edge of the blade it may happen that the secondary particles get a large negative velocity in x-direction and/or a large velocity in y-direction. When this occurs the secondary particles can either cross trajectories in front of the blade or they can move even further upstream back into the mixing plane. To avoid this the secondary particle velocity in x-direction is set to a minimum value of 0 m/s.

5.2.2 Results

The results for run b, i.e. the case with d_p = 20 µm, in partial deposition mode are shown in Fig. 13-18. Fig. 13 and 14 show the 2D fields in the central plane of the TWC and the particle melting ratio, respectively. Fig. 15-18 contain the mass flux of the particles impinging and the melting ratio along each blade's normalized curvilinear abscissa. In these plots the full deposition results and the partial deposition runs are compared.
Comparing the TWC field of the impact model, Fig. 13, with the one without an impact model, Fig. 6, directly shows that including particle rebound/fragmentation has a considerable effect on the obtained density field. In this case the blade surface has been assumed dry, so according to the impact model a large fraction of the ice crystal should rebound or shatter. This is confirmed by the incoming and outgoing mass fluxes being equal (not plotted). The incoming mass flux along the surface of the first stator, Fig. 15, is equal for full and partial deposition, since no secondary particles re-impinge on the first stator vane. The partial deposition mass fluxes for the rotor, Fig. 16, and stator 2, Fig. 17, are higher than the mass fluxes for full deposition. The largest difference is obtained at the trailing edge of the blades where the (smaller) secondary particles hit the surface.
No obvious differences can be observed when the melting ratio field obtained in partial deposition mode, Fig. 14, is compared to the one obtained in full deposition mode, Fig. 8.
The melting ratio along the blades, Fig. 18, confirms this for the first stator as well as for the rotor. Some very small fragmented particles are able to hit the trailing edge surface of stator 2 on the pressure side at $s/c \approx -0.5$ which results in a slightly higher melting ratio in that area.

6 Conclusions

The trajectories of the ice crystals and their impingement have been computed in a 1.5-stage linear cascade. Results have been shown for two different particles, one of diameter 50 µm and the other one of 20 µm diameter, which were subject to phase change on their trajectory.
Partial deposition is not straightforward to implement in an Eulerian method when periodic boundaries or mixing planes are present. In addition, time-consuming procedures have to be used to avoid crossing of particle trajectories.
It is shown that the introduction of a particle impact model has a strong influence on the resulting particle flow field. The rebounded and fragmented particles impact at different areas along the blade surface.
Despite the uncertainty in the applied theoretical models and its parameters, the computation of ice crystal trajectories and impact in a generic turbofan compressor has shown reasonable results. Future work will focus on extension of the impact model to include the effects of erosion and the effect of the liquid wall film by estimating its thickness by means of the wall shear stress. Also a comparison of predictions with results of ice accretion experiments is envisaged, albeit not for this specific test case, to further validate and calibrate the applied numerical simulation method.

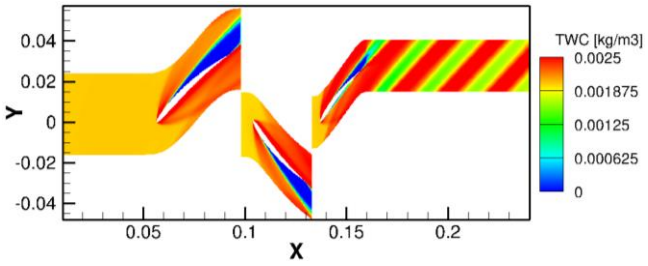

Fig. 13. TWC field run 1b, d_p = 20 µm, impact model activated.

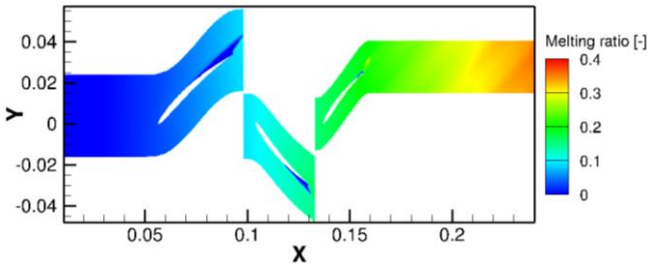

Fig. 14. Melting ratio field run 1b, d_p = 20 µm, impact model activated.

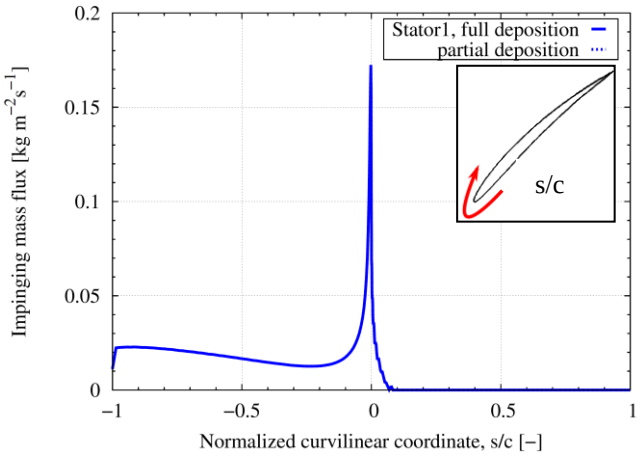

Fig. 15. Mass flux along stator 1.

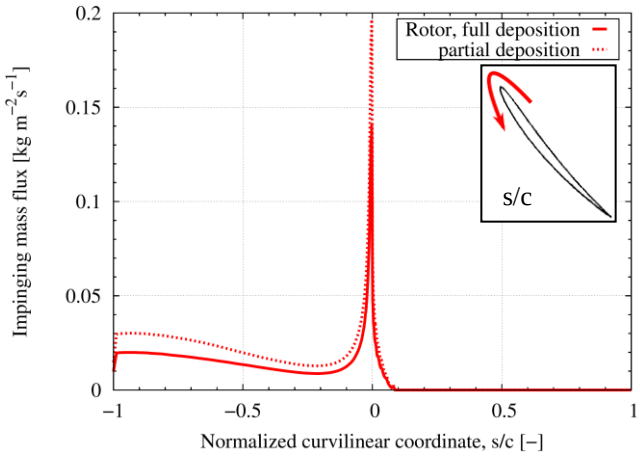

Fig. 16. Mass flux along rotor.

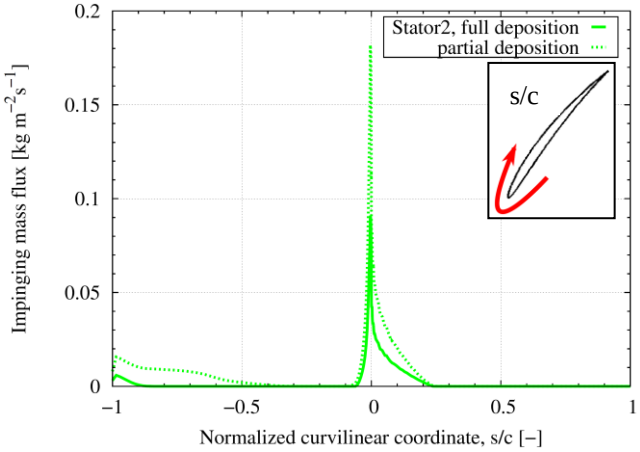

Fig. 17. Mass flux along stator 2.

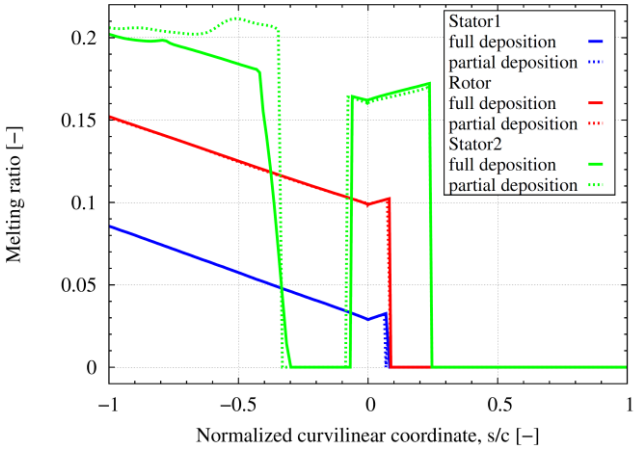

Fig. 18. Melting ratio along blades.

Acknowledgements

This project has received funding from the European Union's Seventh Framework Programme for research, technological development and demonstration under grant agreement n°ACP2-GA-2012-314314.

References

[1] Dezitter F, Grandin A, Brenguier J.-L, Hervy F, Schlager H, Villedieu P and Zalamansky G. HAIC – High Altitude Ice Crystals, *5th AIAA Atmospheric and Space Environments Conference*, San Diego, California, AIAA2013-2674, 2013.

[2] Bravin M, Strapp J and Mason J. An investigation into location and convective lifecycle trends in an ice crystal icing engine event database, *SAE 2015 International Conference on Icing of Aircraft,*

Engines and Structures, Prague, Czech Republic, SAE2015-01-2130, 2015.
[3] Hospers J.M. *Eulerian method for super-cooled large-droplet ice-accretion on aircraft wings*, PhD thesis University of Twente, Enschede, The Netherlands, 2013.
[4] Norde E, Van der Weide E.T.A and Hoeijmakers H.W.M. Eulerian trajectory method and impingement model for non-spherical ice crystals, *9th International Conference on Multiphase Flow*, Firenze, Italy, ICMF2016-366, 2016.
[5] Ganser G.H. A rational approach to drag prediction of spherical and nonspherical particles, *Powder Technology*, Vol. 77, No. 2, pp 143-152, 1993.
[6] Mason B.J. On the melting of hailstones, *Quarterly Journal of the Royal Meteorological Society*, Vol. 82, No. 352, pp 209-216, 1956.
[7] Trontin P, Blanchard G and Villedieu P. A comprehensive numerical model for mixed-phase and glaciated icing conditions, *8th AIAA Atmospheric and Space Environments Conference*, Washington D.C., AIAA2016-3742, 2016.
[8] Hauk T. *Investigation of the impact and melting process of ice particles*, PhD thesis Technische Universität Darmstadt, Darmstadt, Germany, 2015.
[9] Ekici K and Hall K.C. Nonlinear analysis of unsteady flows in multistage turbomachines using harmonic balance, *AIAA Journal*, Vol. 45, No. 5, pp 1047-1057, 2007.
[10] Gopinath A.K, Van der Weide E, Alonso J.J, Jameson A, Ekici K. and Hall K.C. Three-dimensional unsteady multi-stage turbomachinery simulations using the harmonic balance technique, *45th AIAA Aerospace Sciences Meeting and Exhibit*, Reno, Nevada, AIAA2007-892, 2007.
[11] Giangaspero G. *Study of high-order energy-stable discretization techniques for compressible flows*, PhD thesis University of Twente, Enschede, The Netherlands, 2016.

Contact Author Email Address

Ellen Norde, mailto: e.norde@utwente.nl

Copyright Statement